

# A smart nail platform for wireless subsoil health monitoring via unmanned aerial vehicle-assisted radio frequency interrogation

Received: 31 January 2025

Accepted: 11 December 2025

Published online: 27 December 2025


 Check for updates

Yashwanth Ramesh<sup>1,2,6</sup>, Muhammad Masud Rana<sup>1,2,6</sup>, Praveen Srinivasan <sup>1,2</sup>, Akshay Krishnakumar<sup>1,2</sup>, Sarath Gopalakrishnan<sup>1,2</sup>, Jason Adams<sup>3</sup>, Shalamar Armstrong<sup>4</sup> & Rahim Rahimi <sup>1,2,5</sup> 

Monitoring subsoil conditions across large agricultural areas is essential for optimizing resource use and supporting sustainable crop production. However, most existing sensing systems rely on battery-powered electronics that are costly, require maintenance, and are difficult to scale. To address these limitations, we introduce HARVEST (Hybrid Antenna for Radio frequency-enhanced Volumetric water content and Electrical conductivity-based Soil Tracking), a low-cost, wireless platform that eliminates the need for onboard electronics. HARVEST uses nail-shaped sensing probes physically and electrically coupled to a triple-ring antenna positioned above the ground, reducing signal loss while preserving sensitivity to subsurface changes. Variations in soil moisture and salinity modify the electrical characteristics of the buried probes, shifting the antenna's resonant response, which is wirelessly detected by an aerial reader. The system is optimized through electromagnetic simulations and validated through laboratory experiments and full-season field deployment. HARVEST enables reliable detection of subsoil moisture and conductivity with drone-based readout from altitudes up to 1.8 m. This platform provides a scalable, maintenance-free solution for real-time subsoil monitoring, advancing next-generation precision agriculture technologies. By enabling distributed, low-cost sensors across large fields, HARVEST delivers deeper spatial and temporal insight into subsoil conditions, supporting data-driven agricultural management while reducing environmental impact.

Over the past six decades, global agriculture has made remarkable strides, nearly quadrupling grain production—primarily maize, rice, and wheat—with only a modest 37% increase in cultivated land area. This growth met the demands of a rapidly expanding population, raising global average grain yields from 1.6 Mg ha<sup>-1</sup> in 1961 to 4.7 Mg ha<sup>-1</sup> by 2020<sup>1,2</sup>. However, with the global population projected to

reach 9.7 billion by 2050, food production must increase by approximately 70% to meet demand<sup>3</sup>. Traditional agricultural practices are increasingly inadequate, having already contributed to widespread land and water degradation, affecting nearly 38% of arable land<sup>4</sup>. This trajectory underscores the urgent need for resource-efficient and ecologically sustainable farming strategies<sup>5,6</sup>.

A full list of affiliations appears at the end of the paper.  e-mail: [rrahimi@purdue.edu](mailto:rrahimi@purdue.edu)

A central challenge in achieving sustainable intensification is the high spatiotemporal variability of soil properties—such as pH, moisture, and nutrient distribution—which significantly affects input efficiency<sup>7</sup>. For instance, transitioning from 30 m to 1000 m soil moisture resolution can lead to the loss of up to 80% of spatial variability, resulting in major irrigation inefficiencies<sup>8,9</sup>. Similarly, localized soil pH variations of over 2 units within 6–18 m can misguide lime and fertilizer application, ultimately reducing crop yield. Overcoming these limitations requires fine-resolution soil monitoring to support targeted resource delivery and minimize environmental waste<sup>10</sup>.

Precision agriculture has emerged to address these challenges by integrating sensing technologies, data analytics, and automation to optimize input application<sup>11</sup>. Tools such as unmanned aerial vehicles (UAVs), remote sensing platforms, hyperspectral imaging, and in-field wireless IoT sensors have enabled site-specific management strategies<sup>12–17</sup>. Sensor-assisted irrigation alone has been shown to reduce water use by more than 40% compared to conventional methods<sup>18</sup>. Yet, most commercial systems still rely on battery-powered electronics and expensive wireless modules, which limit large-scale deployment due to high cost, power requirements, and maintenance needs<sup>19</sup>. In-situ soil sensors are particularly promising for tracking critical subsurface parameters such as volumetric water content (VWC) and electrical conductivity (EC)—key indicators of moisture level, salinity, and nutrient availability<sup>20–24</sup>. However, commercially available options like the Decagon STE<sup>®</sup> and Sentek Drill & Drop<sup>®</sup> remain costly and difficult to scale, due to their reliance on active circuitry and limited spatial coverage<sup>25,26</sup>. As a result, many agricultural fields are sparsely instrumented, which degrades data quality and undermines precision decision-making<sup>27</sup>.

To address this gap, our group previously introduced a passive, chipless RF backscatter sensor composed of shorted dipole and meander-line resonators, buried entirely beneath the soil surface to monitor VWC. While this approach showed promise, subsurface placement introduced significant RF attenuation, requiring close-range interrogation (<40 cm) and strict angular alignment—factors that limited its practicality for UAV-based readout or scalable deployment<sup>28,29</sup>.

While some efforts have pursued to overcome this challenge by decoupling the sensing element from the RF antenna, many of these solutions adapt conventional RFID-based architectures<sup>30</sup>. These systems commonly include electronic chips that manage signal processing and identification, paired with antennas that extend beyond the sensing medium (e.g., soil or concrete) to enhance wireless communication<sup>31</sup>. While such designs improve read distance, they often require multi-step fabrication, including soldering and chip integration, and introduce higher material and assembly costs—ultimately limiting their feasibility for broad, field-scale deployment<sup>32</sup>.

In this work, we present HARVEST—a passive, chipless RF backscatter platform for subsoil health monitoring that combines a decoupled sensing–antenna architecture with a simplified, chip-free design. By eliminating integrated electronics and minimizing assembly complexity, HARVEST enables low-cost manufacturing, reliable drone-based interrogation, and wide-area deployment without batteries or maintenance. The system integrates nail-shaped sensing probes embedded into the soil for VWC and EC sensing, each electrically coupled to a triple split-ring resonator (SRR) antenna positioned above ground<sup>33</sup>. This hybrid configuration minimizes soil-induced RF losses while preserving subsurface sensitivity.

We design HARVEST's circular SRRs for low-UHF operation and rotational symmetry, enabling orientation-insensitive (yaw-agnostic) communication when a UAV-mounted reader is positioned directly overhead<sup>34–37</sup>. The nail-shaped sensing probes allow for straightforward soil insertion and consistent sensor–soil contact, while the elevated SRR antenna ensures reliable signal transmission. We optimize the system using full-wave electromagnetic simulations and validate its performance in both laboratory and field environments. Field

deployment in Indiana cornfields during a full growing season demonstrates that HARVEST reliably monitors subsoil VWC and EC at 2 m spatial intervals, with successful UAV-based interrogation from altitudes up to 1.8 m. These results highlight how the integration of low-cost RF components with purpose-built sensing interfaces offers a scalable, maintenance-free approach to subsoil monitoring, with strong potential for supporting data-driven precision agriculture.

## Results

### Working principle

The HARVEST platform integrates two primary components: nail-shaped sensing probes that are embedded in the soil for monitoring subsoil VWC and EC, and a circular triple SRR antenna positioned above ground to enable passive, wireless data communication (Fig. 1a). Each probe is fabricated on a printed circuit board (PCB) and contains two parallel electrodes tailored for its specific sensing function.

The EC probe features an unpassivated lower section that remains in direct contact with the soil. This configuration enables interaction with ions in the soil, whereby variations in ionic conductivity modulate the dissipation of surface traveling waves. These changes result in a shift in the effective parallel resistance across the electrodes. In contrast, the VWC probe is fully passivated, preventing direct ionic contact and allowing the dielectric properties of the surrounding soil to influence the capacitance between electrodes. This enables reliable transduction of moisture-dependent dielectric changes into measurable electrical responses. A third reference probe, fabricated without electrodes, is incorporated into the system to serve as a mechanical stabilizer and provide an environmental baseline for signal referencing.

Each of the three probes is electrically interfaced with a corresponding SRR via a PCB card-edge connector. The largest SRR is linked to the EC probe, the intermediate SRR to the VWC probe, and the smallest SRR to the reference probe. Changes in the surrounding subsoil environment result in shifts in the SRR antenna's reflection coefficient spectrum ( $S_{11}$ ), which are analyzed to extract VWC and EC values.

For VWC sensing, changes in soil moisture alter the effective dielectric constant surrounding the probe, thereby modulating the capacitance  $C$  of the SRR circuit. This leads to a resonant frequency shift governed by the equation

$$f_0 = \frac{1}{2\pi\sqrt{LC}} \quad (1)$$

where  $L$  is the inductance and  $C$  the effective capacitance of the VWC-SRR system. As soil moisture increases,  $C$  increases, leading to a lower resonant frequency.

For EC sensing, changes in ionic conductivity affect the effective parallel resistance  $R_{\text{eff}}$ , which in turn modulates the quality factor  $Q$  of the resonance, described by

$$Q = R_{\text{eff}} \cdot \sqrt{\frac{C}{L}} \quad (2)$$

A higher EC decreases  $R_{\text{eff}}$ , lowering the quality factor and resulting in a broader, shallower resonance in the  $S_{11}$  spectrum. To mitigate signal variability arising from environmental and geometric factors such as UAV altitude, antenna misalignment, and soil heterogeneity, HARVEST implements a ratiometric referencing strategy. VWC is extracted by computing the frequency difference between the VWC and reference SRRs, while EC is determined from the amplitude ratio between the EC and reference SRRs. This referencing scheme ensures robust and interpretable sensing in real-world deployment conditions.

Wireless interrogation is conducted by a drone-mounted RF reader, which includes a dual-polarized wideband antenna (half-power beam width  $\approx 35^\circ$ ), a nano vector network analyzer (NanoVNA), and an

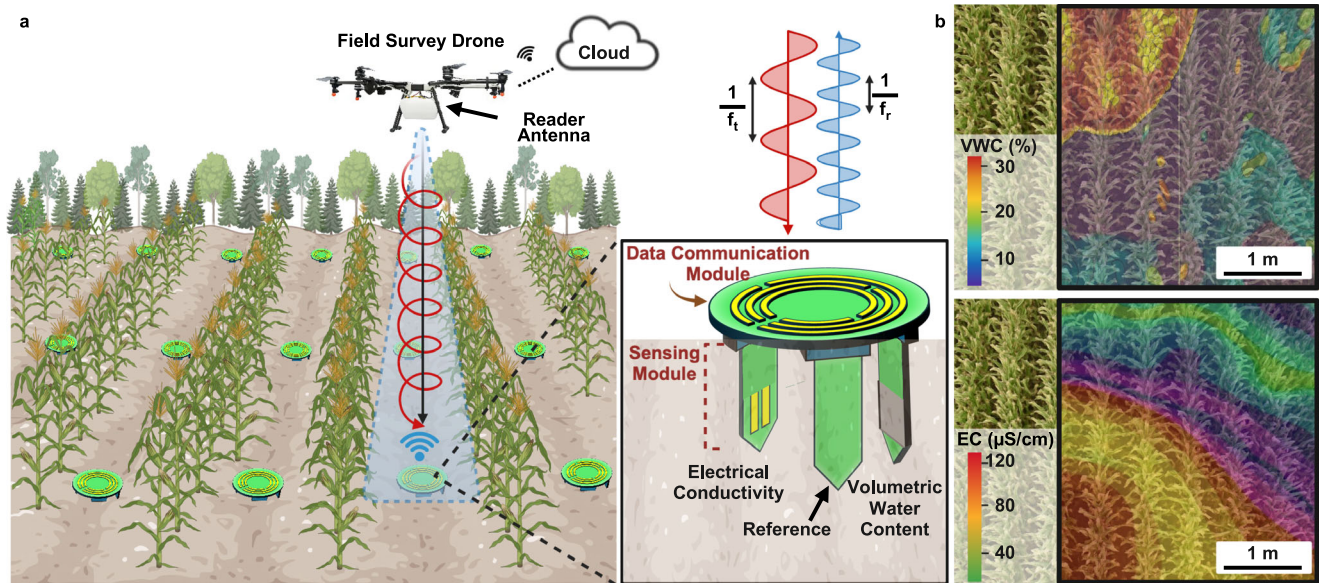


**Fig. 1 | Integrated HARVEST platform for wireless subsoil monitoring.**

**a** Schematic of UAV-assisted RF interrogation of HARVEST sensors deployed across an agricultural field for spatially distributed monitoring. Enlarged view of the HARVEST sensor showing its two key components: the Sensing Module comprising nail-shaped probes embedded in the soil for measuring volumetric water content

(VWC) and electrical conductivity (EC), and the Data Communication Module featuring a circular, triple-SRR antenna for far-field wireless transmission. **b** Illustration of how variations in soil parameters are wirelessly monitored with the HARVEST system and enable spatial mapping of subsoil VWC and EC across fields. Created in BioRender. Rahimi, R. (2025) <https://BioRender.com/cl60guq>.

onboard microcontroller unit (MCU). During operation, the UAV hovers above each sensor and initiates a frequency sweep via the NanoVNA. The  $S_{11}$  response from the sensor reveals three distinct resonance peaks, each corresponding to one of the SRRs: the first peak reflects EC sensing via its amplitude, the second captures VWC sensing via its frequency shift, and the third provides a stable reference.

To suppress environmental RF noise and multipath effects, the UAV system first captures a background spectrum ( $S_{11}^{\text{Background}}$ ) at a nearby sensor-free location. This is subtracted from the spectrum recorded over the sensor ( $S_{11}^{\text{Sensor}}$ ), yielding the calibrated signal

$$S_{11}^{\text{Calibrated}}(\text{dB}) = S_{11}^{\text{Sensor}} - S_{11}^{\text{Background}} \quad (3)$$

The resulting spectrum is smoothed using a Savitzky–Golay filter, which enhances signal fidelity by reducing noise while preserving peak features. All signal processing occurs onboard the UAV in real time. The MCU extracts the relevant resonance features and translates them into VWC and EC values using calibration curves obtained through laboratory characterization. The sensor's location and timestamp are appended to the data, which is then wirelessly uploaded to a secure cloud server via an onboard Wi-Fi module (Fig. 1b). This fully autonomous, real-time workflow enables scalable, maintenance-free monitoring of subsoil health across wide agricultural areas without the need for manual data retrieval or post-processing.

To evaluate the practical implementation of the HARVEST platform for wireless, electronic-free subsoil monitoring, the system was systematically designed and assessed across five key performance domains. First, the triple SRR antenna architecture was optimized to establish three distinct frequency bands corresponding to the individual sensing channels. This ensured minimal spectral crosstalk and stable wireless performance under varying readout angles and environmental conditions. Second, the coupling between the nail-shaped sensing probes and their respective SRRs was characterized to evaluate sensitivity, stability, and repeatability in response to changes in subsoil VWC and EC. Third, the system's readout range and spatial cross-sensitivity were investigated by varying the position and orientation of neighboring sensors, enabling assessment of robustness

under different deployment geometries. Fourth, HARVEST incorporates built-in self-calibration and noise-cancellation strategies—leveraging a dedicated reference SRR and environmental background subtraction—which were validated in both lab and field conditions to ensure consistent signal quality under real-world variations such as drone altitude, antenna orientation, and ambient RF noise. Finally, the complete HARVEST system was deployed in an active cornfield and operated over a full crop growth cycle to validate its long-term field performance and agronomic relevance. Together, these five domains of characterization were employed to rigorously validate the HARVEST platform and demonstrate its effectiveness as a robust, scalable, and maintenance-free solution for wireless subsoil sensing in precision agriculture.

### Antenna design

The wireless communication interface of the HARVEST platform was designed to encode soil parameters into the spectral response of a passive, battery-free antenna system. When interrogated remotely by an RF reader, changes in subsoil conditions—such as VWC and EC—modify the dielectric environment around the antenna, resulting in measurable shifts in its resonant frequency and amplitude. These variations are captured through the antenna's  $S_{11}$ , enabling fully passive, electronic-free sensing without onboard power or circuitry.

To achieve multi-parameter monitoring, the antenna was designed with three distinct resonators: two assigned to subsoil VWC and EC sensing, and one serving as a reference for internal calibration and environmental noise compensation. Ensuring sufficient spectral separation between these resonant peaks was critical to avoid overlap and enable accurate signal decoding. Accordingly, the operating bandwidth of the antenna system was set between 600 and 1200 MHz, with targeted inter-peak separation of 150–200 MHz. This range was chosen based on application-specific constraints and physical design considerations. The 915 MHz center frequency was selected as it falls within the globally recognized Industrial, Scientific, and Medical (ISM) band, which supports unlicensed low-power telemetry applications such as IoT, RFID, and agricultural monitoring. Operating within this band enabled a balance between antenna compactness and signal

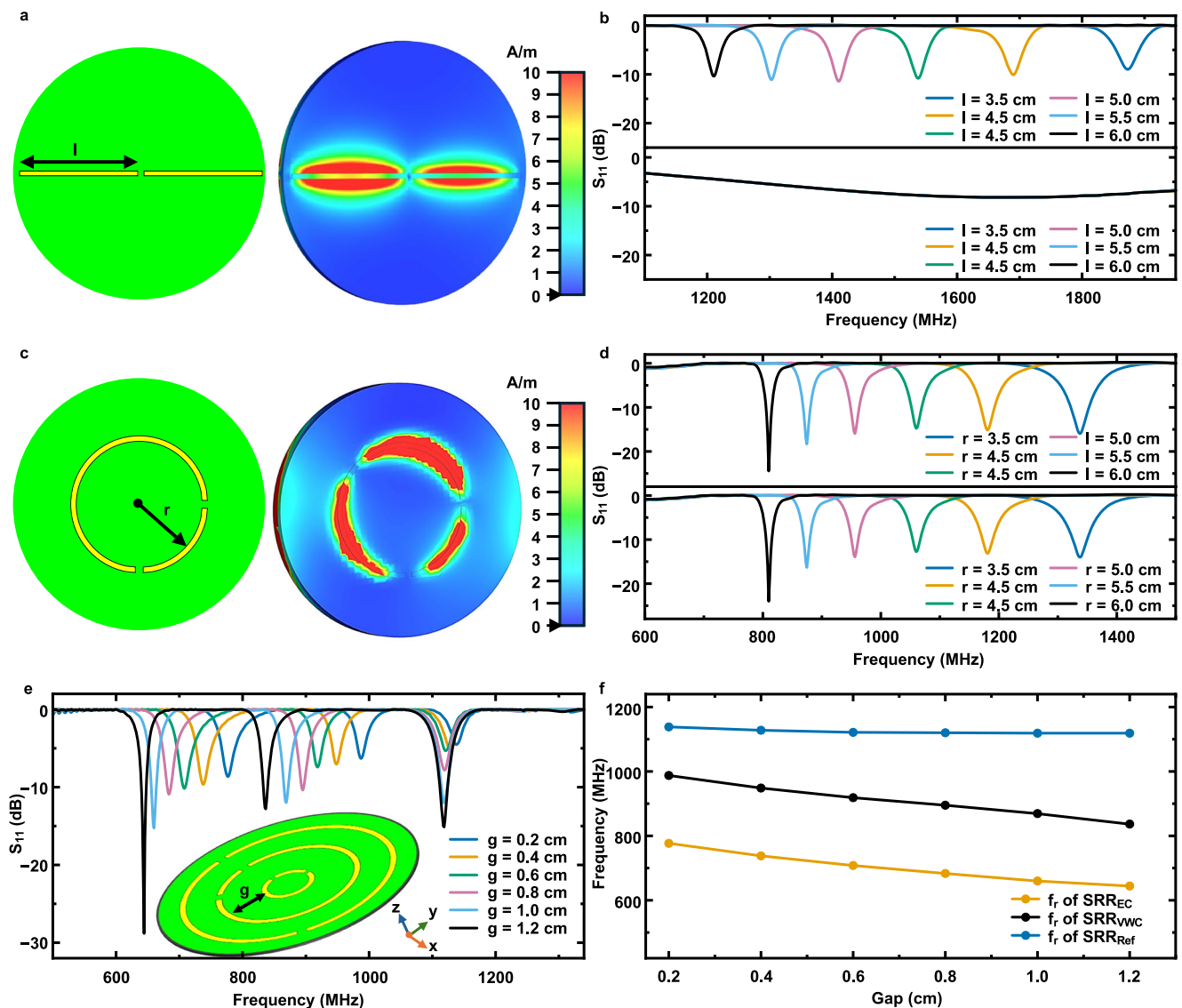


**Fig. 2 | Antenna simulation and SRR design optimization.** **a** Dipole antenna on a circular substrate, shown with simulated magnetic field (H-field) distribution. **b** Simulated reflection coefficient ( $|S_{11}|$ ) of the dipole antenna before and after  $90^\circ$  rotation, across dipole lengths ( $l = 3.5$  cm to  $6$  cm). **c** Single split-ring resonator (SRR) on a circular substrate along with its corresponding H-field distribution. **d** Simulated  $S_{11}$  spectra of the single SRR before and after  $90^\circ$  rotation, evaluated

for resonator radii ( $r = 3.5$  cm to  $6$  cm). **e** Triple-SRR configuration and corresponding  $S_{11}$  spectra recorded at varying inter-resonator gap distances  $g$  are shown as an inset schematic. **f** Resonant frequency shifts of each SRR as the gap distance ( $g = 0.2$  cm to  $1.2$  cm). Source data for Fig. 2 are provided as a Source data file. (a, c: Images used courtesy of ANSYS, Inc.).

propagation performance, especially in dense vegetation. The antenna design also prioritized angular independence to accommodate variability in drone-based interrogation geometry. Initial evaluations using linear dipole resonators revealed substantial angular sensitivity: rotating the dipole by  $90^\circ$  in the azimuthal plane significantly diminished the resonance amplitude across all tested lengths ( $3.5$ – $6.0$  cm), confirming the impracticality of dipole geometries for drone-compatible sensing (Fig. 2a, b).

To overcome this limitation, a circular double-slit SRR configuration was developed, offering improved magnetic field coupling and rotational insensitivity. Parametric simulations across SRR radii from  $3.5$  to  $6.0$  cm demonstrated predictable resonance shifts from  $1375$  to  $800$  MHz, with only  $\pm 21$  MHz deviation under  $90^\circ$  rotation, an acceptable tolerance for field deployment (Fig. 2c, d).

Building on these results, a composite antenna structure was designed using three concentric SRRs of varying radii, enabling simultaneous detection of EC, VWC, and a stable reference signal

within the specified  $600$ – $1200$  MHz window. This multi-resonant triple SRR antenna exhibited strong isolation between resonators, minimal spectral crosstalk, and robust backscattering performance under varying reader rotation angles when reader is aligned above the sensor. The largest SRR was connected to the EC probe, the middle to the VWC probe, and the smallest to the reference probe. To ensure long-range communication even through dense corn canopy (up to  $1.8$  m height), the antenna was designed with high directivity. The induced surface magnetic fields, current distributions, and directional radiation patterns of the final antenna assembly are illustrated in Supplementary Fig. 1. The interrogator, mounted on the UAV, operated at  $-10$  dBm—well below the FCC limit of  $30$  dBm—ensuring safe, low-interference operation.

To determine the optimal configuration for the triple SRR antenna, a systematic parametric analysis was conducted. An SRR with a radius of  $4$  cm was first selected as the baseline reference resonator, exhibiting a primary resonance at  $1150$  MHz. Subsequently, the spacing

between adjacent SRRs was varied from 0.2 cm to 1.2 cm to assess its effect on resonance behavior and to determine the ideal radii for the remaining two SRRs (Fig. 2e). Simulation results revealed that increasing the inter-resonator spacing led to the emergence of three distinct resonance peaks. While the third peak (corresponding to the reference SRR) remained largely unaffected, the resonant frequencies of the first and second peaks showed a -10% shift with increasing spacing (Fig. 2e). Notably, the  $|S_{11}|$  of all three peaks increased significantly with greater spacing, indicating reduced electromagnetic coupling and minimized crosstalk between the SRRs. The trends observed in Fig. 2e are summarized in Fig. 2f, which describes the resonance frequencies of the three SRRs as a function of spacing. At the minimum spacing of 0.2 cm, the resonances occurred at approximately 1120 MHz, 950 MHz, and 790 MHz. As the spacing increased, these frequencies diverged, particularly for the two larger SRRs. The smallest SRR (lowest frequency) exhibited frequency stabilization once the spacing exceeded 0.8 cm, maintaining consistent performance. At a spacing of 0.8 cm, the separation between the resonant peaks reached a favorable configuration, with the first and second peaks separated by 200 MHz and the second and third peaks by 168 MHz—all within the target operational bandwidth of 600–1200 MHz. This configuration provided sufficient spectral isolation for accurate sensing while preserving compact antenna dimensions. Based on these results, a spacing of 0.8 cm between SRRs was selected as the optimal design for achieving robust, multi-resonant wireless sensing with minimal interference.

### Antenna-sensor integration and sensitivity performance assessment

Initially, the nail-shaped sensing probe design was analysed through systematic simulations that varied the electrode configuration to maximize sensitivity to dielectric changes in the surrounding soil. A parametric sweep of electrode widths and gaps was then carried out to examine their effect on the electric field distribution and the resulting impedance response. Simulations across soil conditions ranging from dry to wet conditions showed that electrodes with a width of 10 mm and a gap of 8 mm consistently observing the maximum relative change in electrical impedance, establishing this geometry as the most effective for capturing soil moisture dynamics with high sensitivity (Supplementary Fig. 2). Next, to evaluate the performance of the integrated hybrid probe-antenna sensor, the effect of connecting the nail probes to the triple SRR antenna was systematically analyzed. As shown in Fig. 3a, attaching the reference probe (which lacks electrodes) to the smallest resonator had no measurable impact on the resonance spectrum. In contrast, connecting the VWC probe to the middle SRR resulted in a -3% reduction in its resonant frequency, while the other two peaks remained unchanged. Similarly, coupling the EC probe to the largest SRR caused a -1% shift in the resonant frequency of the corresponding peak. These results, as summarized in Fig. 3b confirm that each probe-resonator pair operates independently, with negligible crosstalk or spectral interference. Supplementary Fig. 3 illustrates changes in surface magnetic fields, current distributions, and radiation directivity upon probe attachment to the triple SRR antenna. From an equivalent circuit perspective, the frequency shifts observed upon sensor connection can be attributed to the increased effective capacitance introduced by the nail-shaped probes. This added capacitance slightly lowers the natural resonance frequency of the corresponding SRR, as expected in resonant LC systems. To further characterize HARVEST's sensing response to soil conditions, simulations were performed using a loamy soil model to assess sensitivity to changes in VWC and EC. The VWC probe required electrical passivation to enable capacitive coupling while preventing ionic conduction between the electrodes and soil. This passivation layer is critical not only for electrical isolation, but also for ensuring sensitivity and manufacturability using standard PCB-compatible techniques.

To identify the optimal dielectric coating, simulations were conducted with coating thicknesses ranging from 10  $\mu\text{m}$  to 100  $\mu\text{m}$  applied to the probe's active region. Thinner coatings (10–30  $\mu\text{m}$ ) provided higher sensitivity due to enhanced fringe-field coupling between the electrodes and surrounding soil. However, such coatings posed manufacturing challenges: they exhibited poor uniformity, pinholes, and a higher risk of dielectric failure. Conversely, thicker coatings (e.g., 100  $\mu\text{m}$ ) offered reliable insulation and better  $S_{11}$  but reduced sensitivity to soil VWC due to limited electric field penetration. A 50  $\mu\text{m}$  thick passivation layer was found to offer the best trade-off—providing high sensitivity to changes in soil dielectric properties, robust electrical insulation, and practical manufacturability using scalable, additive techniques such as doctor blade coating with PCB solder mask. This optimized coating was subsequently adopted in the fabrication of the VWC probe and validated through simulation and experimental testing (see Supplementary Note 1 and Supplementary Fig. 4).

The effect of embedding the HARVEST sensor in soil was analyzed by simulating changes in the spectral characteristics—both frequency and intensity—of the backscattered signal's  $S_{11}$  under varying soil conditions. When the sensor was placed in the soil model with the nail probes buried and the triple SRR antenna above ground, a -1 dB reduction in  $|S_{11}|$  was observed in the received signal. This was attributed to dielectric losses within the soil medium, which slightly reduced the quality factor (Q-factor) of the resonator response.

To evaluate sensitivity to VWC, simulations were conducted in which the soil's VWC was increased from 0% to 25% in 5% increments, while keeping the EC constant. The results showed that the middle resonant peak—associated with the VWC sensing probe—underwent a 5.7% downshift in resonant frequency and a -45% decrease in  $|S_{11}|$  amplitude with each 5% increase in soil VWC (Fig. 3c, d). In contrast, the other two peaks—corresponding to the EC and reference resonators—remained stable, exhibiting minimal frequency shifts ( $\pm 6$  MHz) and negligible amplitude changes.

A separate set of simulations was performed to assess sensitivity to soil EC. Here, the VWC was held constant at 5%, while EC was varied from 0.01 to 0.8 dS/m in 0.2 dS/m steps. These simulations revealed that the first resonant peak (associated with the EC sensor) experienced a -33% decrease in  $|S_{11}|$  with each incremental increase in EC, while its resonant frequency remained effectively unchanged ( $\pm 2$  MHz). Again, the VWC and reference resonant peaks showed minimal variations in both frequency and amplitude under EC modulation (Fig. 3e, f).

These results confirm that HARVEST's multi-resonator design enables selective and independent monitoring of VWC and EC. The platform demonstrated linear sensitivities of approximately: 7.32 MHz per % VWC (captured through frequency shift of the middle SRR) and 4.32 dB per dS/m EC (captured through amplitude change of the first SRR). Importantly, the reference resonator consistently maintained its resonant frequency and amplitude across all environmental variations, validating its role as a stable in-situ calibration standard for signal normalization and drift correction. This ensures the robustness and reliability of HARVEST under variable field conditions and highlights the value of the triple-resonator configuration for multi-parameter subsoil monitoring.

### Readout range and spatial cross-sensitivity

To assess the practical readout range and field-deployability of the HARVEST platform using a portable UAV-mounted interrogation system, both simulations and controlled in-lab experiments were performed. These studies employed two types of antennas: a standard high-gain horn reader antenna (HRA) and a custom-developed portable reader antenna (PRA). In both setups, the HARVEST platform—comprising a triple-SRR antenna with nail-shaped sensing probe connections—was positioned inside a soil model, and the reflected  $S_{11}$  spectral signals were captured and analyzed.

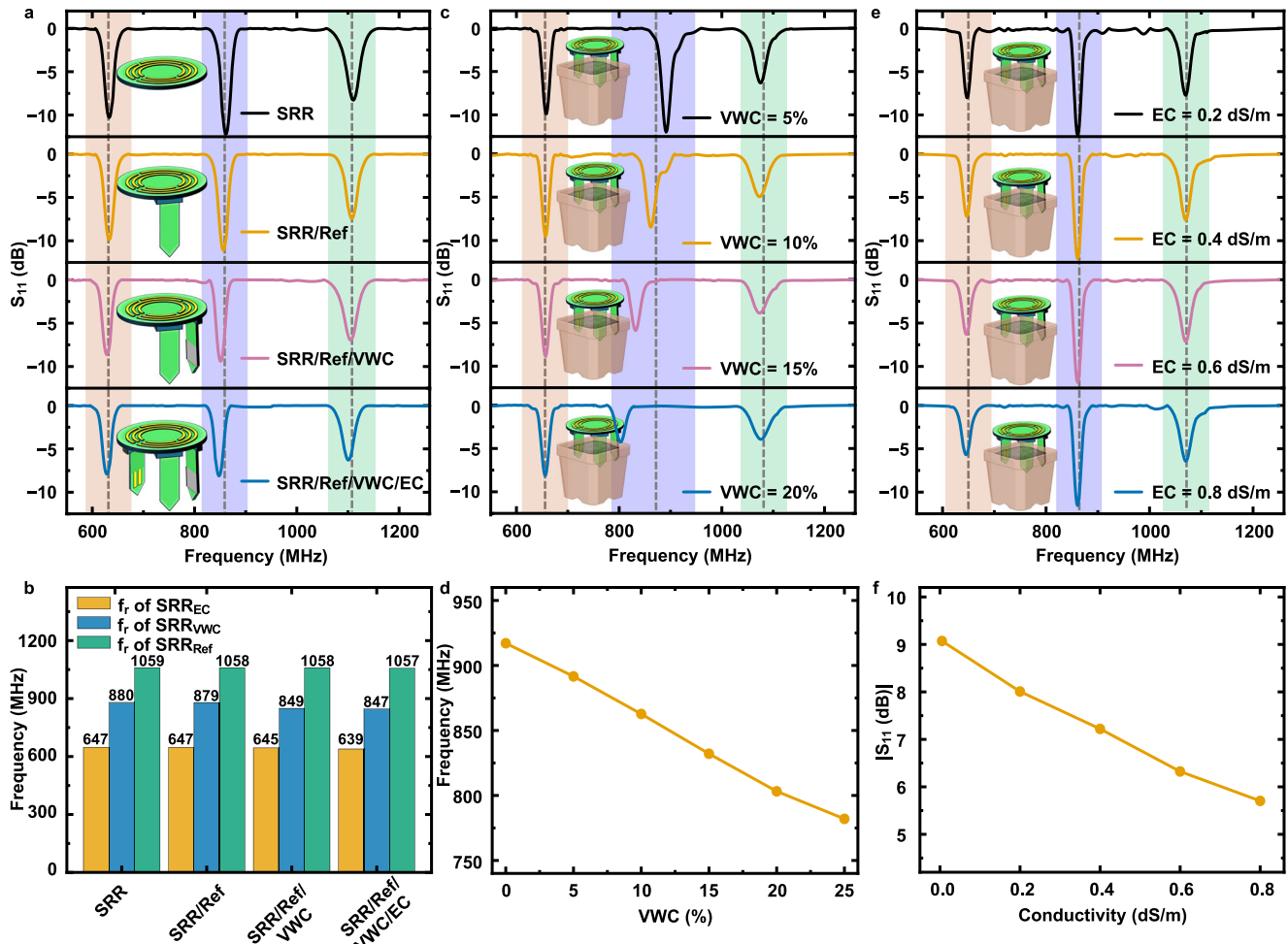


**Fig. 3 | Simulation-based characterization of HARVEST’s sensitivity to changes in soil VWC and EC.** **a** Variation in the  $S_{11}$  spectra as each nail probe—reference, VWC, and EC—was successively connected to its designated SRR on the antenna. **b** Recorded resonant frequencies for each SRR upon successive integration of the reference, VWC, and EC monitoring probes. **c** Changes in the  $S_{11}$  spectra when HARVEST was embedded in soil and VWC was incrementally increased from 5% to 20% insets (a–c): illustrates the different stages of sensor probes attachment and placement in various soil conditions. **d** Calibration curve showing the frequency

shift of the VWC-associated SRR (middle peak,  $SRR_{VWC}$ ) as a function of VWC. **e** Changes in the  $S_{11}$  spectra when HARVEST was placed in soil with EC varied from 0.2 to 0.8  $dS\ m^{-1}$ . **f** Calibration curve showing the change in amplitude of the EC-associated SRR (first peak,  $SRR_{EC}$ ) as a function of EC. (Color-coded resonance peaks in spectra: Orange: EC resonator ( $SRR_{EC}$ ), Blue: VWC resonator ( $SRR_{VWC}$ ), Green: Reference resonator ( $SRR_{Ref}$ )). Source data for Fig. 3 are provided as a Source Data file. Plant pot icons: Created in BioRender. Rahimi, R. (2025) <https://BioRender.com/bSeqfj>.

Simulations were first conducted by varying the distance between the reader antenna and the HARVEST sensor from 60 cm to 180 cm in 30 cm increments. The lower bound of 60 cm was intentionally selected to exceed the triple SRR antenna’s far-field limit of 58 cm, ensuring meaningful far-field analysis. The soil model was kept at a constant VWC of 5%. As shown in Fig. 4a, the resonant frequency positions of the three SRRs remained stable across all distances. However, a progressive reduction in peak amplitude was observed with increasing distance, as expected from free-space path loss and reduced coupling efficiency.

These simulations were then validated experimentally. In-lab  $S_{11}$  spectral measurements from the HARVEST platform using both the HRA and PRA yielded results that closely matched simulation outputs, with deviations in resonant frequencies limited to  $\pm 1.4\%$  for the HRA and  $\pm 3\%$  for the PRA. The resonance peak positions remained consistent across all read distances for both interrogators, while the signal intensity gradually decreased. Importantly, in all scenarios, the received signals remained above the system’s noise threshold of  $-2.5$  dB up to a distance of 180 cm, confirming the platform’s effective wireless readability at practical UAV heights (Fig. 4b, c).

To address environmental variability in the field—including fluctuations in UAV altitude and azimuth orientation, multipath interference, and background RF noise—two complementary signal stabilization strategies were implemented. First, a self-calibrating reference resonator was incorporated. This third SRR is connected to an electrically isolated, non-penetrating nail probe that is unaffected by soil VWC or EC. Because it remains stable regardless of environmental changes, this SRR enables a ratiometric sensing approach by serving as a consistent internal baseline across measurements.

To evaluate the effectiveness of this ratiometric approach, the  $|S_{11}|$  amplitude ratios of the first (EC) and second (VWC) resonant peaks relative to the third reference peak were calculated over the entire 60–180 cm readout range. These ratios remained constant across distances and interrogator types. Specifically, simulation results yielded  $|S_{11}|_{EC}/|S_{11}|_{Ref} = 2.8 \pm 0.1$  and  $|S_{11}|_{VWC}/|S_{11}|_{Ref} = 2.2 \pm 0.1$ . Experimental results using the HRA produced similar ratios of  $3.1 \pm 0.1$  for EC and  $2.2 \pm 0.12$  for VWC. When using the PRA, the values were  $3.1 \pm 0.15$  for EC and  $2.2 \pm 0.16$  for VWC. This consistency highlights the robustness of the ratiometric method and its capacity to mitigate signal variation due to distance or antenna characteristics. Notably, throughout all simulated and

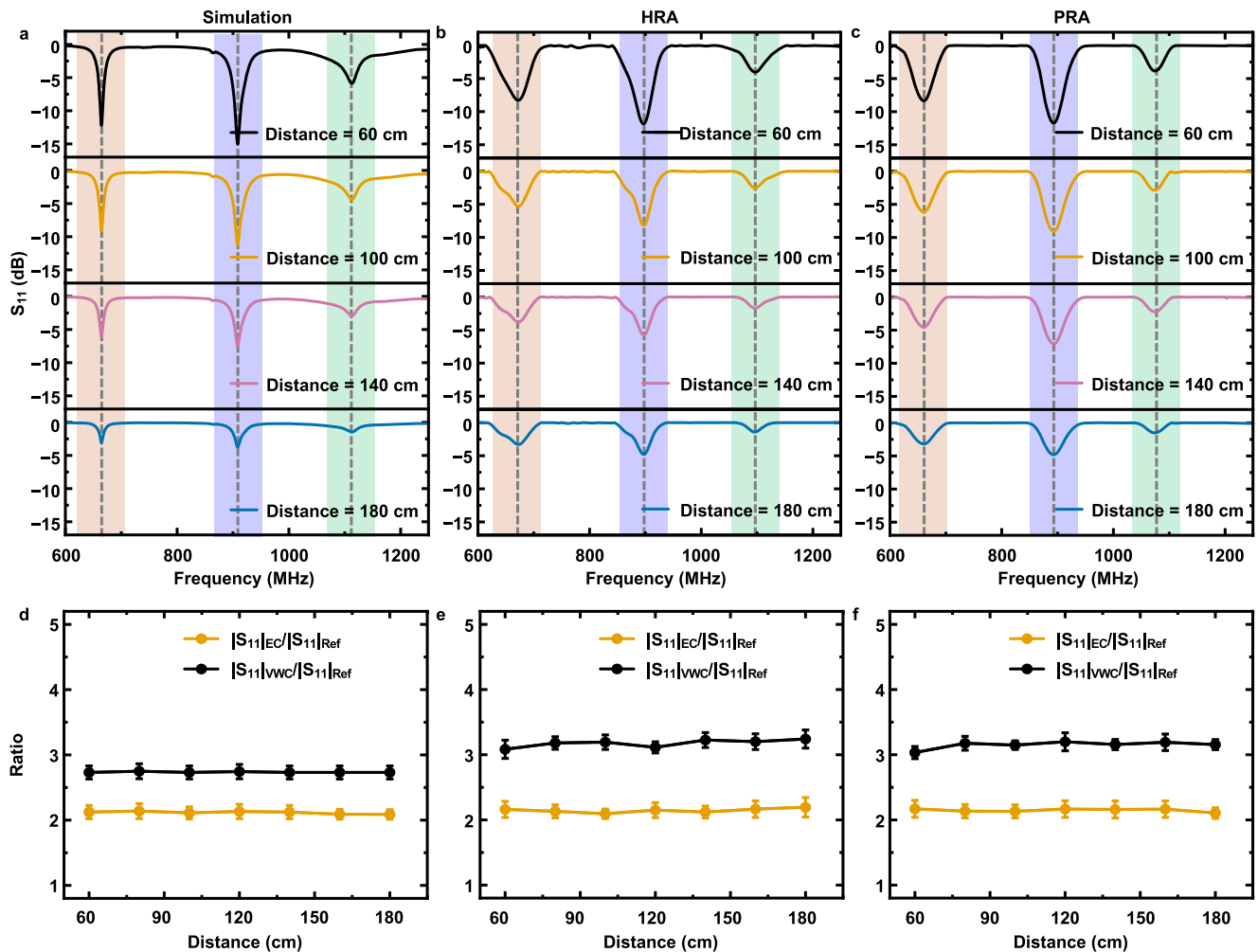


**Fig. 4 | Read range characterization of the HARVEST system.** Changes in the recorded  $S_{11}$  spectra were measured as the distance between the HARVEST sensor and the reader was varied using three different RF interrogator configurations: **a** Simulated excitation using a waveguide port. **b** Experimental testing with an external Horn Reference Antenna (HRA). **c** Experimental testing using a Portable Reader Antenna (PRA). The amplitude ratios of the VWC resonator ( $SRR_{VWC}$ ) and EC resonator ( $SRR_{EC}$ ) were compared to the reference resonator ( $SRR_{Ref}$ ) at

varying RF interrogator distances for: **d** Waveguide port simulation, **e** HRA-based experimental interrogation, and **f** PRA-based experimental interrogation. (Color-coded resonance peaks in spectra: Orange: EC resonator ( $SRR_{EC}$ ), Blue: VWC resonator ( $SRR_{VWC}$ ), Green: Reference resonator ( $SRR_{Ref}$ )). **d**, **e**, **f** Error bars indicate the standard deviation based on five independent measurements. Source data for Fig. 4 are provided as a Source data file.

experimental distance variations, the soil VWC and EC were kept constant, ensuring that any variation in the absolute signal amplitudes was solely due to readout distance. The ratiometric approach, by referencing the signal amplitudes to the stable, environmentally isolated third SRR, maintained consistent measurement outputs, confirming the method's reliability and independence from readout range variations (Fig. 4d-f).

The second stabilization method involved differential background subtraction followed by spectral filtering. Each UAV sensing operation consisted of two consecutive measurements: a background spectrum recorded with the UAV-mounted RF reader hovering over an empty region of the field (without the HARVEST sensor), and a sensor-inclusive spectrum recorded when the UAV repositioned directly above the sensor. The calibrated  $S_{11}$  response was then obtained by subtracting the background spectrum from the sensor-inclusive measurement using the Eq. (3). This subtraction technique effectively removed location-specific reflection artifacts and isolated the sensor's actual resonant response. To further refine the signal, Savitzky-Golay filtering was applied to smooth high-frequency noise while preserving the shape and location of the resonance peaks, as illustrated in Supplementary Note 2 and Supplementary Fig. 5.

Together, the self-calibrating reference SRR and background subtraction strategy form a robust signal processing pipeline. This combined approach ensures that the HARVEST platform delivers high-fidelity frequency and amplitude readings, even under variable UAV positions and fluctuating RF environments, thereby enabling reliable field deployment for passive wireless subsoil monitoring.

After finalizing the sensor's readout range and verifying its in-situ calibration capability, it was necessary to determine the minimum separation distance required between adjacent HARVEST platforms to avoid electromagnetic crosstalk during wireless interrogation. This assessment ensured that individual sensors could be accurately read without interference from nearby units. To conduct this test, one HARVEST platform was interrogated from a fixed distance of 180 cm using the high-gain horn antenna (HRA), while a second identical HARVEST unit was placed at varying lateral separations ranging from 0 to 3.5 m relative to the first. At each distance, the backscattered  $S_{11}$  spectra from the fixed sensor were recorded and analyzed to extract the quality (Q) factors of the three resonant peaks.

Significant spectral distortion and peak broadening were observed when the two HARVEST units were positioned within 0–1 m of each other, indicating strong mutual coupling and signal

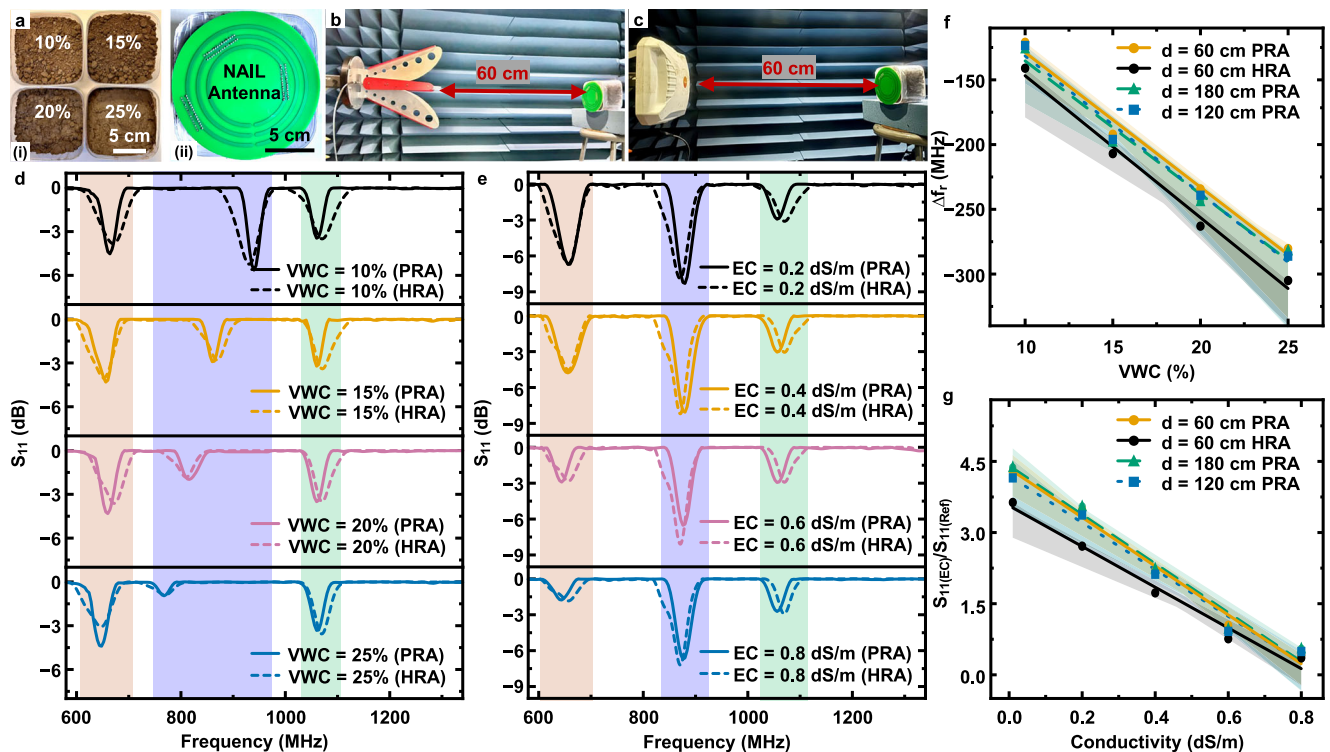


**Fig. 5 | In-lab characterization of HARVEST sensor sensitivity to soil VWC and EC.** **a** (i) Top view of prepared soil samples with varying VWC levels of 10%, 15%, 20%, and 25%; (ii) Placement of HARVEST sensor within the soil sample. **b** Wireless measurement setup using a Horn Reference Antenna (HRA) and **c** Portable Reader Antenna (PRA) as RF interrogator inside an anechoic chamber. Calibrated  $S_{11}$  spectral responses of HARVEST with **d** varying VWCs (10%–25%) and **e** ECs (0.01–0.8 dS/m) using both HRA and PRA. **f** Calibration curve showing the differential resonant frequency shift of the VWC resonator ( $SRR_{VWC}$ ) relative to the reference

resonator ( $SRR_{Ref}$ ) as a function of VWC for different read distances. **g** Relative change in peak amplitude of the EC resonator ( $SRR_{EC}$ ) normalized to the reference resonator ( $SRR_{Ref}$ ) as a function of EC for different read distances. (Color-coded resonance peaks in spectra: Orange: EC resonator ( $SRR_{EC}$ ), Blue: VWC resonator ( $SRR_{VWC}$ ), Green: Reference resonator ( $SRR_{Ref}$ )). **f, g**: Shaded region represents the 95% CI of the linear fit. Source data for Fig. 5 are provided as a Source data file.

interference. However, once the lateral spacing reached 2 m or more, the resonant peaks regained sharpness, and the Q-factors stabilized, demonstrating the suppression of cross-coupling effects. These results establish that a minimum spacing of 2 m between HARVEST sensors is necessary to ensure electromagnetic isolation and preserve signal fidelity during sequential or parallel field deployments. Additional details are provided in Supplementary Note 3 and Supplementary Fig. 6.

Following the assessment of HARVEST's wireless readout range and validation of its in-situ self-calibrating and spectral filtering methodology, the system's sensitivity to variations in soil VWC and EC was evaluated. In this analysis, the frequency shift of the VWC-specific resonator was calculated relative to the reference SRR, while the impact of soil EC was quantified through the amplitude ratio between the EC-specific resonator and the reference resonator. The performance of these sensitivity metrics was assessed using both the HRA and the PRA, as shown in Fig. 5.

To test VWC sensitivity, soil samples with VWCs ranging from 10% to 25% were prepared and the HARVEST sensor was positioned into the soil samples such that the nail probes were inside the soil and the triple SRR antenna was outside soil facing the interrogating antenna (Fig. 5a). In parallel, for EC sensitivity testing, a separate set of samples was prepared with fixed VWC (8%) and EC values varying from 0.01 to 0.8 dS/m. The experimental configuration and the relative positioning of the RF reader and sensor setup are illustrated in Fig. 5b, c. The corresponding  $S_{11}$  spectra from the HARVEST platform under different VWCs are presented in Fig. 5d.

As soil VWC increased from 10% to 25%, a clear 17% downshift in the resonant frequency of the middle peak (VWC SRR) was observed,

along with a gradual reduction in amplitude. In contrast, the reference and EC resonator peaks remained relatively stable with less than  $\pm 2.45\%$  deviation. For EC sensitivity evaluation, increasing the soil EC up to 0.8 dS/m resulted in a 77% drop in the amplitude of the first resonant peak (EC SRR), while its frequency remained constant (Fig. 5e). Notably, both the reference and VWC resonator peaks remained unaffected across this EC range. These spectral characteristics were consistently observed using both the HRA and PRA interrogation systems.

The extracted calibration curves for soil VWC and EC are shown in Fig. 5f, g. For VWC monitoring, the differential frequency shift between the VWC and reference resonators displayed a linear trend with a sensitivity of 9.45 MHz/% (Adj.  $R^2 = 0.94$ ), and a standard deviation of  $\pm 1.45\%$  across read distances of 60, 120, and 180 cm. For EC monitoring, the ratio of peak amplitudes between the EC and reference resonators also showed a linear response of 4.34 dB/(dS m<sup>-1</sup>) (Adj.  $R^2 = 0.95$ ), with a standard deviation of  $\pm 1.83\%$  across the same read distances. These results confirm not only the high sensitivity and robustness of the HARVEST platform but also the efficacy of its self-calibration framework to maintain measurement accuracy across varying interrogation distances.

### Field deployment and agronomic validation

To validate the long-term performance, durability, and agronomic applicability of the HARVEST platform under realistic field conditions, a complete wireless sensor network was deployed in an active cornfield and operated throughout a full crop growth cycle. The goal was to evaluate the system's ability to perform continuous, maintenance-free

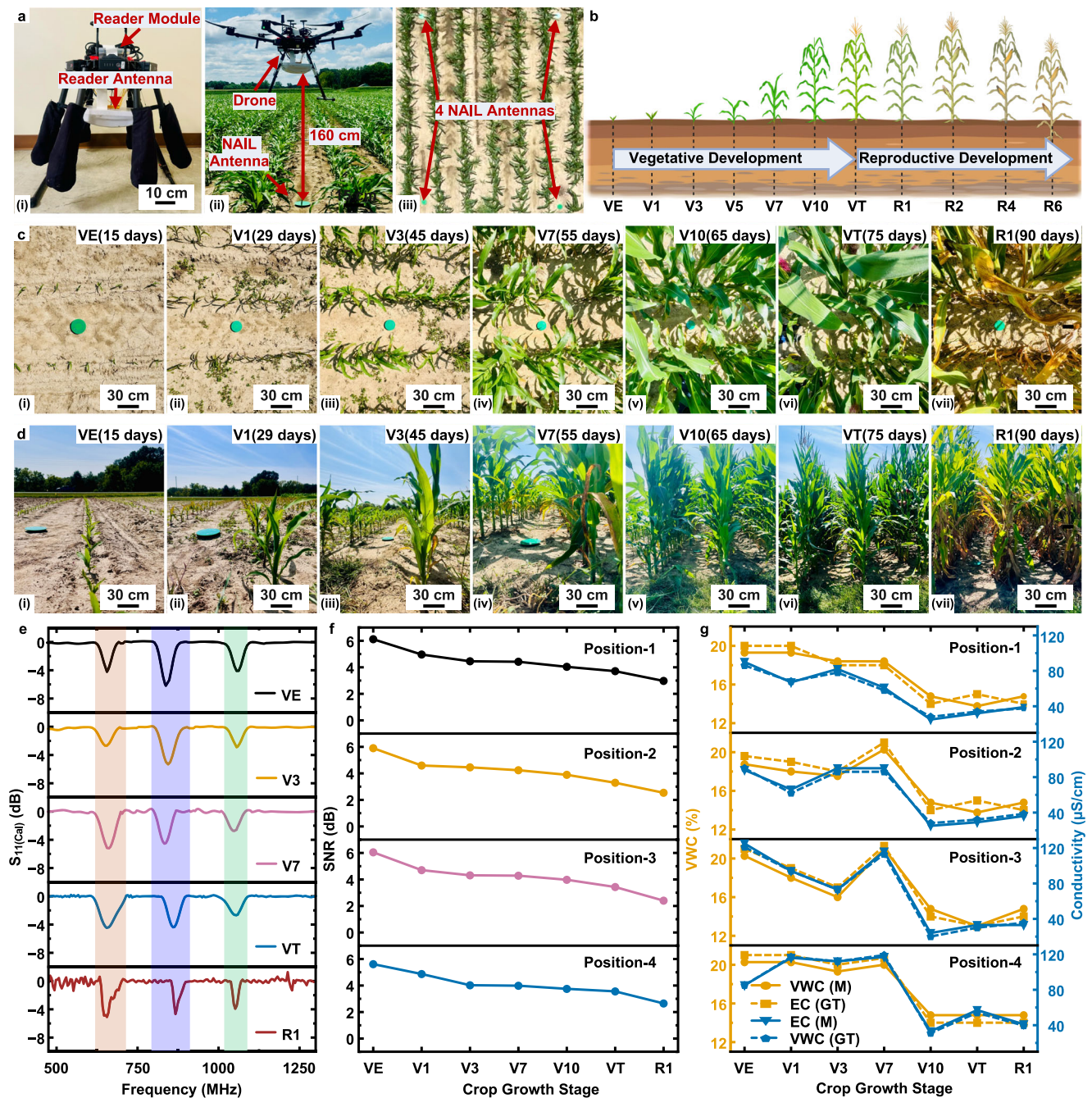


**Fig. 6 | UAV-assisted in-field measurements of HARVEST during a full corn crop cycle.** **a** (i) Photograph of the portable reader module mounted on a drone; (ii) Drone-mounted reader hovering above the HARVEST system at Position 1 in the cornfield; (iii) Aerial view showing four deployment positions of HARVEST systems within the cornfield, each co-located with commercial TERS-12 soil probes for ground-truth measurements. **b** Schematic of the corn growth cycle, highlighting different vegetative and reproductive stages. Created in BioRender. Rahimi, R. (2025) <https://BioRender.com/6z5xcv0>. **c** (i–viii) Aerial views and **d** (i–viii) side views of HARVEST units captured at Position 1 across multiple crop growth stages.

**e** The  $S_{11}$  spectra of HARVEST recorded at different crop growth stages. **f** Corresponding Signal-to-Noise Ratio (SNR) recorded from UAV-based measurements at Position 1 at different crop growth stages. **g** Temporal profiles of soil WWC and EC recorded by HARVEST (measured-M) across four field positions throughout the crop cycle, compared with ground-truth (GT) data from TERS-12 probes. (Color-coded resonance peaks in spectra: Orange: EC resonator ( $SRR_{EC}$ ), Blue: WVC resonator ( $SRR_{WVC}$ ), Green: Reference resonator ( $SRR_{Ref}$ )). Source data for Fig. 6 are provided as a Source data file.

monitoring of subsoil WVC and EC under dynamic environmental and agricultural conditions.

A customized readout unit was mounted on a DJI Mavic-series drone. This setup included the PRA affixed beneath the drone between the landing gear and connected to a NanoVNA interfaced with a microcontroller housed in a lightweight acrylic enclosure on top of the drone (Fig. 6a(i)). During field data collection, the drone hovered

vertically above each HARVEST unit for approximately five seconds per measurement, ensuring a stable line-of-sight (LOS) communication channel (Fig. 6a(ii)). A camera mounted to the underside of the drone recorded overhead images to document sensor positioning and visibility throughout crop development (Fig. 6a(iii)).

Four HARVEST units were deployed 10 m apart within an operational cornfield at the Agronomy Center for Research and Education

(ACRE) at Purdue University (610 Purdue Mall, West Lafayette, IN 47907). This spacing was selected to reflect the heterogeneous nature of croplands and ensure spatially resolved measurements across different microenvironments. Each unit was embedded with its nail-shaped sensing probes vertically inserted into the subsoil, while the triple SRR antenna was positioned exposed above ground for wireless interrogation.

The field deployment spanned the majority of the crop's growth cycle, beginning in the early vegetative (VE) stage and continuing into the reproductive (R1) phase. As shown in Fig. 6b, corn development stages progressed from emergence (VE) through tasseling (VT) to early kernel development (R1). Visual observations of the field, from both overhead and side perspectives (Fig. 6c, d), confirmed that increasing foliage height (from 5 cm to 170 cm) progressively reduced visibility and LOS between the drone reader and HARVEST units. The back-scattered signal's spectra collected at sensor position 1 during this period showed increasing noise levels as the canopy thickened (Fig. 6e). The decline in signal quality is quantified in Fig. 6f, where the signal-to-noise ratio (SNR) dropped from  $5.6 \pm 0.2$  dB during the VE stage to 4 dB by V3, plateauing at  $3.6 \pm 0.3$  dB through VT. By R1, all four sensors exhibited a -2 dB SNR reduction due to canopy interference. Nevertheless, all three resonant peaks remained distinguishable, indicating that HARVEST's readout capacity was sufficient for reliable soil monitoring up to the R1 stage.

To validate sensor accuracy, in-field soil VWC and EC data from the HARVEST system were benchmarked against ground-truth measurements collected using commercial TEROs-12 sensors and a wired data-logger (Fig. 6g). From VE to V7, VWC at positions 1 and 4 remained stable around  $20 \pm 2\%$ , while positions 2 and 3 exhibited a 4% decline followed by a sharp increase, indicative of localized drying and rehydration. Similarly, EC values at positions 1–3 followed a comparable trajectory, whereas position 4 started at a lower baseline of  $80 \pm 15 \mu\text{S cm}^{-1}$ . These variations underscore HARVEST's ability to detect localized soil heterogeneity. Between V7 and V10, a pronounced decline in both VWC (-4%) and EC ( $-80 \mu\text{S cm}^{-1}$ ) was observed at positions 2–4, likely reflecting increased root water and nutrient uptake. Position 1, in contrast, showed a more gradual decline. From V10 to R1, VWC dropped during tasseling and subsequently recovered across positions 1–3, while position 4 remained stable at -14%. For EC, positions 1–3 showed gradual increases ( $-20$  to  $40 \mu\text{S cm}^{-1}$ ), whereas position 4 experienced a sharp rise followed by a matching drop. Quantitatively, HARVEST measurements showed close agreement with ground-truth data. Deviations in VWC and EC remained within  $2.42 \pm 1.86\%$  and  $3.12 \pm 1.32\%$ , respectively, throughout the entire monitoring period.

Despite being spaced just 10 m apart, the four HARVEST sensor units captured up to 35% variability in subsoil VWC and EC, highlighting the critical need for high-resolution, spatially distributed soil sensing in precision agriculture. Throughout the UAV-based field measurements, HARVEST demonstrated a polarization-insensitive response. Regardless of the incident wave polarization (vertical or horizontal) from the UAV-mounted reader, the triple SRR antenna consistently exhibited clear and distinguishable resonant responses to changes in both VWC and EC. This behavior suggests a quasi-circular polarization pattern of the antenna, which supports stable wireless interrogation from UAVs across a range of azimuthal orientations, as further detailed in Supplementary Note 4 and Supplementary Fig. 7.

The system also proved capable of overcoming potential installation-related artifacts, particularly those involving air gaps between the nail probes and soil matrix, which can otherwise hinder electrical contact and degrade sensing accuracy. Experimental characterization showed that either compacting the soil manually during burial or allowing a natural rain event to settle the soil around the nail probes effectively eliminated air gaps. This self-correcting behavior led to stable and consistent long-term measurements, even when minor air gaps were present during initial installation (see Supplementary

Note 5 and Supplementary Fig. 8). Importantly, HARVEST achieved performance comparable to commercial soil probes—which often rely on wired connections and bulky data loggers—but with a much simpler and scalable design. Unlike traditional systems, HARVEST is fully passive, battery-free, and UAV-compatible, enabling rapid, flyover-based scanning of large sensor networks with dual-parameter sensing (VWC and EC) in a compact and maintenance-free form factor. These capabilities make HARVEST especially well-suited for large-scale deployments in smart farming, supporting cost-effective, real-time monitoring of soil conditions critical for precision irrigation and salinity management.

## Discussion

Monitoring subsoil VWC and EC is critical for evaluating root-zone conditions that govern plant water uptake, nutrient transport, and salinity stress. Among available technologies, passive wireless sensing—especially RFID-based systems—offers a promising path toward scalable, low-cost, and distributed soil monitoring without the need for embedded electronics or batteries. These systems generally fall into two categories: chipped sensors that utilize application-specific integrated circuits (ASICs), and chipless RFID sensors, which encode information directly through resonator geometry or material-dependent electromagnetic properties.

Several prior works have explored these approaches. For example, Kim et al. developed an inkjet-printed chipped RFID soil moisture sensor for cost-effective agricultural monitoring. Their device achieved a read range of -1.5 m in air, with the sensing interdigitated electrodes (IDEs) buried 5 cm below the soil surface. Sensing relied on moisture-induced capacitance changes that modulated the chip's backscatter response<sup>38</sup>. In another example, Fonseca et al. demonstrated a UHF RFID sensor completely buried 1 cm underground, with a read range of -1.2 m<sup>39</sup>. While both systems were functional, their reliance on ASICs introduces complexity, power constraints, and higher cost.

To address these limitations, the chipless RFID paradigm eliminates ASICs and instead encodes sensing information via intrinsic changes in the electromagnetic response of the tag. Our group previously reported on such approaches, utilizing passive resonators (e.g., short dipole and meander-line designs) to detect VWC through frequency shifts. Although those systems demonstrated strong linearity, their performance was limited by soil dielectric loss, requiring shallow burial (<5 cm) and maintaining a short interrogation distance (~40 cm). Furthermore, chipless RFID sensors often face additional challenges, including limited resolution, narrow bandwidth, and dependence on reader orientation—making them less reliable under real-world field conditions.

In response, this work introduces HARVEST: a fully passive, chipless, wireless sensing platform designed for robust, multi-parameter subsoil monitoring. HARVEST features a bifurcated architecture where nail-shaped sensing probes interface with an above-ground, triple SRR antenna for wireless interrogation. This separation improves electromagnetic coupling and reduces signal attenuation from surrounding soil. The HARVEST platform was validated through a complete pipeline—from electromagnetic simulation, in-lab characterization using a portable reader, and finally real-world deployment in a live cornfield over an entire growing season using a custom UAV-mounted interrogator.

The sensor exhibited sensitivities of -9.45 MHz/% for VWC and -4.32 dB/dS·m<sup>-1</sup> for EC, comparable to or exceeding the performance of commercial soil probes and previously reported RFID-based solutions (Supplementary Tables 1 and 2). Critically, this sensing capability was achieved using a fully passive, chipless design, at an estimated unit cost of \$1–\$3, representing significant cost reduction relative to conventional active or RFID-based probes (Supplementary cost analysis information and Table 3).

The bifurcated sensor–antenna layout enabled reliable wireless readout from up to 1.8 m above ground, while the sensing probes remained buried at root-zone depths. Despite using a sequential interrogation scheme, scan times were compatible with UAV workflows. For example, a 1-acre field (~4000 m<sup>2</sup>) instrumented with ~63 HARVEST units spaced 10 m apart could be fully scanned in approximately 13 min (Supplementary Note 6 and Supplementary Fig. 9). This performance is competitive with state-of-the-art RFID systems, which often suffer from shorter read distances or require surface-near deployment.

Importantly, this work spans the full spectrum from resonator-level electromagnetic design to field-scale validation. The HARVEST system was deployed across the entire corn crop phenological stages, enabling spatiotemporal mapping of VWC and EC with high resolution. The robustness of the platform was confirmed even in the presence of increasing plant canopy and variable soil conditions.

Nonetheless, some limitations and practical considerations remain. First, UAV interrogation requires precise vertical alignment with the above-ground antenna; misalignment reduces signal strength and impairs resonance detection. This challenge became more pronounced during later crop stages (e.g., R1), where increased canopy height reduced the SNR. Second, weather conditions such as wind or rain can disrupt UAV stability and affect measurement consistency<sup>40</sup>. Third, long-term deployment in heterogeneous soils may result in probe fouling, degradation, or detuning over time.

To address these challenges, several future improvements can be envisioned. UAV navigation can be enhanced through adaptive flight path control and real-time feedback for alignment correction<sup>41</sup>. Matched filtering centered around expected resonance frequencies can boost SNR in high-loss environments<sup>42</sup>. Material durability can be improved through superhydrophobic coatings, streamlined geometries to reduce fouling, and robust encapsulation. Resonator performance can be further optimized by exploring low-loss substrates, multi-layer architectures, and higher-Q structures<sup>43–45</sup>. Beyond technical enhancements, HARVEST can be extended toward multi-modal sensing (e.g., pH, temperature, microbial activity), beamforming, and frequency-division multiplexing to support even denser deployments<sup>46,47</sup>. Data generated by HARVEST could also be integrated into variable rate agronomy platforms, enabling real-time interventions such as targeted irrigation or nutrient application<sup>48</sup>. The ability to detect spatial anomalies in subsoil VWC and EC, even within short distances (e.g., 10 m), illustrates the critical need for dense, distributed, and autonomous sensing infrastructure in precision agriculture. In summary, HARVEST presents a scalable, ultra-low-cost, and chipless wireless soil monitoring platform capable of robust dual-parameter sensing. Its passive nature, UAV compatibility, and strong field validation position it as a transformative solution for next-generation digital agriculture, capable of improving resource efficiency, reducing environmental impact, and supporting food security for a growing global population.

## Methods

### Electromagnetic simulation

The HARVEST sensor integrates three nail-shaped sensing probes with a circular triple SRR antenna to wirelessly monitor soil EC and VWC. The antenna comprises three concentric, equally spaced circular SRRs fabricated on a circular FR-4 PCB substrate ( $\epsilon_r = 4.25$ ,  $\tan \delta = 0.02$ ). Each SRR was formed by introducing a split into a closed-loop annular resonator, establishing localized capacitive elements at the gaps. The nail probes, also FR-4-based PCBs shaped like nails, contain two parallel gold-electroplated copper electrodes along their length to serve as in-situ soil sensors.

To optimize the physical dimensions and inter-element spacing of both the SRRs and the nail probe electrodes, detailed electromagnetic simulations were conducted using ANSYS HFSS 2024 R1 with its 3D

finite element method (FEM) solver. A tetrahedral mesh of 125,342 cells was used for the high-frequency simulations, with waveguide ports aligned along the  $Z$  axis and positioned at varying heights above the antenna to emulate UAV-based RF interrogation. These configurations were used to extract the far-field  $S_{11}$  parameters of the triple SRR antenna.

The nail probes were simulated separately using ANSYS's Maxwell low-frequency solver with a mesh of 5000 tetrahedral cells. A 1 V excitation potential was applied across the electrode terminals to evaluate the electric field distribution and impedance characteristics. Once characterized, the probes were virtually integrated into the antenna model to simulate full-system behavior.

The operational frequency range for the HARVEST system was set between 600 and 1200 MHz (within the UHF band) to minimize attenuation through soil. To resolve three distinct resonance peaks (corresponding to reference, VWC, and EC measurements), the SRR radii were parameterized between 3 and 6 cm, and the spacing between them from 0.2 to 1.2 cm. Multiple iterative simulations were conducted to determine optimal values. Each SRR contained six slits arranged in two patterns: one tri-phase set (at 0°, 110°, and 210°) allowed nail probe integration, while a second set of vertical slits mitigated shorting when the probes were inserted into soil.

The nail probe electrode geometry and spacing, as well as the PCB substrate dimensions, were also optimized in the ANSYS's Maxwell solver. To ensure robust electrical connectivity between the nail probes and their corresponding SRRs, coaxial connectors were modeled at the copper trace interface. Their radii were parameterized to achieve impedance-matched signal transmission between the nail electrodes and SRRs. Specifically, the smallest SRR was linked to a non-functional nail (no electrodes) for reference, the middle SRR to a VWC-sensing nail with a solder mask-covered passivation region, and the largest SRR to an EC-sensing nail without passivation—allowing direct soil-electrode contact.

Full-system simulations were carried out in two stages: first in air, then with a layered soil model representing realistic deployment conditions, in which the nail probes were embedded underground, and the antenna remained above the surface. To model how VWC affects dielectric properties, the Topp equation was used to relate soil VWC to its effective permittivity ( $\epsilon_{eff}$ ). Simulations were performed across VWC levels from 0% to 25%, analyzing corresponding shifts in the resonant frequency ( $f_r$ ). To model soil conductivity, the material's dielectric loss (loss tangent) was varied based on known correlations with conductivity (measured at 900 MHz). A range of soil conductivities from 0.01 to 0.8 dS m<sup>-1</sup> was simulated to evaluate its impact on  $|S_{11}|$ . Finally, to assess the system's angular sensitivity to drone azimuthal orientation, the RF waveguide port position is fixed while the sensor is rotated azimuthally from 0° to 180° in 30° increments. Simulation results (refer to Supplementary Fig. 10) confirm that HARVEST maintains stable VWC and EC readouts across a range of UAV azimuthal angles when positioned directly above the sensor, exhibiting minimal signal degradation or resonance distortion.

### Sensor fabrication

The fabrication of the HARVEST sensor, including both the nail-shaped probes and the triple-SRR antenna, was carried out using standard PCB manufacturing techniques based on the optimized geometries established from electromagnetic simulations. To establish connectivity between the antenna and nail probes, a 5530841-2 PCB card edge connector (CONN SEC II 15 POS 100 C/L, TE Connectivity, Schaffhausen, Switzerland) was soldered to the antenna using electroplated plated-through holes drilled through the PCB. These holes connected the bottom-mounted connector to the top-side SRRs, enabling each nail probe to be linked to its corresponding resonator.

The antenna design included a ground plane beneath the FR-4 substrate to suppress back-lobe radiation and shield the SRRs from

electromagnetic interference originating from the soil. To further isolate the system from the environment, the backside of the antenna, including the ground plane, was coated with a 500  $\mu\text{m}$ -thick solder mask that served as a passivation barrier. This ensured there was no direct electrical or physical contact between the ground plane and the soil, preserving the resonance characteristics of the SRRs during operation in moist environments. A 500  $\mu\text{m}$ -thick bead of UV-curable solder mask (TMYLOKU, China) was applied to the interconnect regions of the VWC and EC nail sensors using a Nordson Ultimius V EFD fluid dispenser (Westlake, OH, USA), operating at a speed of 30 mm/s and pressure of 10 psi. The dispensed mask was cured under a Sun Ray UV floodlight (Uvitron International, West Springfield, MA, USA) for 30 min, yielding a conformal dielectric encapsulation layer. To enhance capacitive sensitivity for VWC measurements, the active sensing area of the VWC nail was further coated with an additional 50  $\mu\text{m}$ -thick solder mask layer, providing dielectric isolation while maintaining effective capacitive coupling with surrounding soil VWC. In contrast, the active area of the EC nail was deliberately left uncovered to ensure direct electrical contact with the soil, enabling accurate EC sensing. This passivation strategy not only ensured consistent dielectric performance but also protected the sensor from fouling and degradation in field deployments.

For long-term environmental robustness, both the top and bottom surfaces of the triple SRR antenna were coated with a 25  $\mu\text{m}$ -thick Teflon hydrophobic dielectric layer. This hydrophobic coating served dual purposes: it prevented environmental contamination of the exposed top-side antenna traces and electrically isolated the bottom ground plane to avoid short circuits due to moisture infiltration from the soil. Upon completing passivation and coating steps, both the sensor and antenna components were thoroughly rinsed with ethanol and deionized water, dried using nitrogen, and stored under ambient conditions for future deployment (refer to Supplementary Fig. 11 for images of the fabricated nail probes, antenna, and the fully assembled HARVEST system).

### Portable reader module development and implementation

The readout system was customized into a compact, modular, lightweight, and drone-compatible unit for conducting wireless measurements of the fabricated device. The custom reader module was built in a modular design, incorporating a Raspberry Pi Pico W MCU, which was connected to a portable nanoVNA (NanoVNA-H, Seesii). The NanoVNA is a dual-port transmission and reflection VNA that consists of an RF signal generator, a directional coupler, and an RF receiver. It operates with three distinct signal generators: an S15351 for low-frequency operations up to 140 MHz, and two ADF4350 RF synthesizers to extend the frequency range up to 1500 MHz, delivering a maximum RF output power of +10 dBm. The RF receiver chain includes an AD8342 mixer coupled with a baseband amplifier, which down-converts the RF signal to an intermediate frequency (IF) of approximately 12 kHz. This IF signal is digitized using 12-bit analog-to-digital converters (ADCs) integrated into the GD32 MCU, where the firmware precisely computes the phase and magnitude of the signal, ensuring accurate spectrum analysis across the wide frequency range. The NanoVNA was connected to an XPOL V2 PRA, which was mounted on the drone's underside. The XPOL V2 antenna offers a wideband coverage from 617 to 4200 MHz with a peak gain of -11 dBi. It features a  $2 \times 2$  MIMO antenna with a HPBW almost equal  $35^\circ$  along with two cross-polarized ports in a rugged, IP65-rated enclosure, making it suitable for outdoor and aerial deployment. For data acquisition, the NanoVNA was interfaced to a Raspberry Pi Pico W, responsible for collecting the backscattered signal's resonance characteristics and wirelessly transmitting it to a cloud database (For additional details on the data acquisition process and the conversion of spectral responses to subsoil VWC and EC values, please refer to Supplementary Note 7 and Supplementary Fig. 12). The Raspberry Pi Pico W offers a compact,

cost-effective platform with low power consumption, dual-core real-time processing, and seamless MicroPython support, making it ideal for reliable wireless data acquisition. Its built-in Wi-Fi, easy GPIO control, and MCU-based stability further enhance its suitability for space-constrained, battery-powered applications. It features an onboard Infineon CYW43439 wireless chip and supports Wi-Fi 4 (802.11n) wireless networks. The two ADF4350 RF synthesizers were interfaced with the TX and RX pins of the Raspberry Pi Pico W to facilitate communication via the I2C protocol. The Raspberry Pi Pico W and the NanoVNA were assembled, enclosed, and securely mounted on the top side of the drone to ensure stability during both flight and hovering.

### Soil sample preparation

In order to validate the simulation results, the HARVEST sensor was tested in soil samples sourced from ACRE at Purdue University. After collection, the soil was ground to achieve a uniformly textured consistency with smaller particle sizes and divided into separate portions for VWC and EC experiments. Initially, to test the sensor's response to varying VWCs without altering the soil's natural EC, increasing volumes of deionized (DI) water (500 ml, 1000 ml, 1500 ml, and 2000 ml) were incrementally added to four portions of soil and thoroughly mixed. This process produced soil samples with VWCs of 10%, 15%, 20%, and 25%, which were verified using a commercial TEROS 12 (METER Group Inc) soil sensor. On the other hand, to assess the sensor's performance under varying ECs, a saline stock solution was prepared by dissolving 275 mg of a salt mixture comprising sodium chloride, calcium chloride, and magnesium chloride (Sigma-Aldrich, St. Louis, MO, USA) in 500 ml of DI water. These solutions were added in equal volumes to four equal portions of soil, each with a nearly constant VWC of 5%, and thoroughly mixed to ensure uniform salt distribution. This led to soil samples with ECs 0.2, 0.4, 0.6, and 0.8  $\text{dSm}^{-1}$ , which were later verified using the TEROS 12 sensor to confirm accuracy. This systematic preparation of soil samples with controlled VWCs and ECs created realistic testing conditions, enabling a comprehensive evaluation of the sensors' performance in detecting variations in soil properties.

### Anechoic chamber measurements

Initial measurements in an anechoic chamber were used in evaluating the HARVEST sensor's performance under conditions with minimal electromagnetic interference and optimal echo suppression. This setup facilitates a more accurate comparison between the simulation results and the results acquired from the in-lab characterization of the proposed sensor. The performance of the proposed soil sensor was initially tested with an ETS Lindgren 3164-10 quad ridge dual-polarized horn antenna coupled to a Keysight E5072A VNA (Santa Rosa, CA, USA). During the experiments, the sensor was positioned in the soil container such that the nail probes were completely buried in it and the triple SRR antenna was facing the horn antenna. To first determine the maximum read distance of the proposed sensor, the horn antenna was positioned on an ETS Lindgren linear slider capable of linearly moving to 200 cm from its original position. The distance between the horn antenna and the sensor in the soil container was varied in constant increments, and the sensor's  $S_{11}$  was recorded at each interval to determine the sensor's maximum read distance. To observe the sensor's sensitivity in soil samples of varying VWCs, the sensor was placed in the soil samples prepared, and the corresponding  $S_{11}$  was recorded. A similar approach was taken to measure the sensor's sensitivity to varying soil EC. The whole procedure was repeated, this time using an XPOL V2 portable antenna connected to a Nano VNA as the RF source. This was done to gauge the effectiveness of the custom-developed portable reader. The GT soil VWC and soil EC values were acquired via a TEROS 12 sensor. The TEROS 12 sensor was interfaced with an Arduino MKR1010 data logger, and the soil VWC and EC values were recorded from various points within the same soil container to ensure uniformity. The recorded baseline values were then correlated with the

resonant characteristics obtained from the PRA to develop a calibration curve.

### In-field measurements

To assess the sensitivity of the wireless passive soil sensors in a real-world environment, the sensors were deployed at four predetermined locations (40° 28' 4.95" N, 86° 59' 10.42" W; 40° 28' 13.06" N, 86° 59' 42.29" W; 40° 28' 13.05" N, 86° 59' 42.21" W; and 40° 28' 12.99" N, 86° 59' 42.20" W) within a cornfield at ACRE at Purdue University. Prior to sensor deployment, soil VWC and EC values were measured using the TERSO12 sensor to establish baseline GT data. The TERSO 12 sensor was interfaced with Arduino MKR1010 data logger, and the soil VWC and EC values were recorded from various points surrounding the point of sensor deployment. The sensors were then inserted into the soil, ensuring the nail probes were fully buried while the antenna was oriented upward. A portable antenna was mounted on the underside of a drone by securing it between its landing support legs. The MCU unit and NanoVNA, connected to the antenna and housed in an acrylic box, were placed on top of the drone to reduce noise caused by turbulence. The drone-mounted reader was flown over each sensor at the four locations for an average duration of 10 s, and the reflection characteristics of each sensor were recorded. This data was acquired throughout the majority of the corn crop's growth cycle to ensure the wireless passive soil sensor's consistency, reliability, and to emphasize its practical applicability.

### Data availability

All data supporting the findings of this study are available within the article and its supplementary files. Any additional requests for information can be directed to and will be fulfilled by the corresponding authors. Source data are provided with this paper.

### Code availability

Codes for data acquisition and postprocessing for the HARVEST readout unit used in this study are available on GitHub<sup>49</sup> (<https://github.com/yashu-R/HARVEST-Subsoil-Health-Monitoring>).

### References

1. Bindraban, P. S. & Rabbinge, R. Megatrends in agriculture—views for discontinuities in past and future developments. *Glob. Food Secur.* **1**, 99–105 (2012).
2. Abdo, A. I. et al. Conventional agriculture increases global warming while decreasing system sustainability. *Nat. Clim. Chang* **15**, 110–117 (2024).
3. Elferink, M. & Schierhorn, F. Global demand for food is rising. Can we meet it? *Harv. Bus. Rev.* **7**, 04 (2016).
4. Corwin, D. L. & Lesch, S. M. Apparent soil electrical conductivity measurements in agriculture. *Comput Electron Agric.* **46**, 11–43 (2005).
5. Valin, H. et al. The future of food demand: understanding differences in global economic models. *Agric. Econ.* **45**, 51–67 (2014).
6. Cassman, K. G. What do we need to know about global food security?. *Glob. Food Secur.* **1**, 81–82 (2012).
7. McLaughlin, D. & Kinzelbach, W. Food security and sustainable resource management. *Water Resour. Res.* **51**, 4966–4985 (2015).
8. Qadir, M., Boers, T. M., Schubert, S., Ghafoor, A. & Murtaza, G. Agricultural water management in water-starved countries: challenges and opportunities. *Agric. Water Manag.* **62**, 165–185 (2003).
9. Vergopolan, N. et al. High-resolution soil moisture data reveal complex multi-scale spatial variability across the United States. *Geophys. Res. Lett.* **49**, e2022GL098586 (2022).
10. Li, J., Richter, D., de, B., Mendoza, A. & Heine, P. Effects of land-use history on soil spatial heterogeneity of macro- and trace elements in the Southern Piedmont, USA. *Geoderma* **156**, 60–73 (2010).
11. Zhang, N., Wang, M. & Wang, N. Precision agriculture—a worldwide overview. *Comput. Electron. Agric.* **36**, 113–132 (2002).
12. Stafford, J. V. Implementing precision agriculture in the 21st century. *J. Agric. Eng. Res.* **76**, 267–275 (2000).
13. Yang, C., Everitt, J. H., Du, Q., Luo, B. & Chanussot, J. Using high-resolution airborne and satellite imagery to assess crop growth and yield variability for precision agriculture. *Proc. IEEE* **101**, 582–592 (2013).
14. Di Gennaro, S. F. et al. Spectral comparison of UAV-based hyper and multispectral cameras for precision viticulture. *Remote Sens.* **14**, 449 (2022).
15. Yu, H., Kong, B., Wang, G., Du, R. & Qie, G. Prediction of soil properties using a hyperspectral remote sensing method. *Arch. Agron. Soil Sci.* **64**, 546–559 (2018).
16. Syrový, T. et al. Fully printed disposable IoT soil moisture sensors for precision agriculture. *Chemosensors* **8**, 1–14 (2020).
17. Babaeian, E. et al. Ground, proximal, and satellite remote sensing of soil moisture. *Rev. Geophys.* **57**, 530–616 (2019).
18. Alborno, C. & Giraldo, L. F. Trajectory design for efficient crop irrigation with a UAV. In *proc. IEEE 3rd Colombian Conference on Automatic Control (CCAC)* 1–6 (IEEE, 2017).
19. Marios, S. & Georgiou, J. Precision agriculture: challenges in sensors and electronics for real-time soil and plant monitoring. In *proc. IEEE Biomedical Circuits and Systems Conference (BioCAS)* 1–4 (IEEE, 2017).
20. Walker, J. P., Willgoose, G. R. & Kalma, J. D. In situ measurement of soil moisture: a comparison of techniques. *J. Hydrol.* **293**, 85–99 (2004).
21. Wu, X. & Liu, M. In-situ soil moisture sensing: measurement scheduling and estimation using compressive sensing. In *Proc. ACM/IEEE International Conference on Information Processing in Sensor Networks* 1–12 (IEEE, 2012).
22. Franko, U. & Mirschel, W. Integration of a crop growth model with a model of soil dynamics. *Agron. J.* **93**, 666–670 (2001).
23. Marschner, P. & Rengel, Z. Nutrient availability in soils. In *Mineral Nutrition of Higher Plants* 315–330 Ch. 12 (Academic Press, 2012).
24. Lund, E. D., Colin, P. E., Christy, D. & Drummond, P. E. Applying soil electrical conductivity technology to precision agriculture. In *Proc. Fourth International Conference on Precision Agriculture* (eds Robert, P. C., Rust, R. H. & Larson, W. E.) (ASA, CSSA, and SSSA Books, 1999).
25. Visconti, F., de Paz, J. M., Martínez, D. & Molina, M. J. Laboratory and field assessment of the capacitance sensors Decagon 10HS and 5TE for estimating the water content of irrigated soils. *Agric. Water Manag.* **132**, 111–119 (2014).
26. Segovia-Cardozo, D. A., Franco, L. & Provenzano, G. Detecting crop water requirement indicators in irrigated agroecosystems from soil water content profiles: an application for a citrus orchard. *Sci. Total Environ.* **806**, 150492 (2022).
27. Xu, Z. et al. Flat thin mm-sized soil moisture sensor (MSMS) fabricated by gold compact discs etching for real-time in situ profiling. *Sens. Actuators B Chem.* **255**, 1166–1172 (2018).
28. Gopalakrishnan, S. et al. Battery-less wireless chipless sensor tag for subsoil moisture monitoring. *IEEE Sens. J.* **21**, 6071–6082 (2021).
29. Gopalakrishnan, S. et al. A biodegradable chipless sensor for wireless subsoil health monitoring. *Sci. Rep.* **12**, 1–12 (2022).
30. Hasan, A., Bhattacharyya, R. & Sarma, S. E. Towards pervasive soil moisture sensing using RFID tag antenna-based sensors. In *Proc. IEEE Int. Conf. RFID-Technology and Applications (RFID-TA)*, (IEEE, 2015).
31. Hasan, A. Bhattacharyya, R. & Sarma, S. E. A monopole-coupled RFID sensor for pervasive soil moisture monitoring. In *Proc. IEEE Antennas and Propagation Society International Symposium (APSURSI)* (IEEE, 2013).

32. Alsultan, M. A., Melià-Seguí, J., Parrón-Granados, J. & López-Soriano, S. A battery-less UHF RFID sensor for soil moisture monitoring. *IEEE J. Radio Frequency Identif.* **9**, 286–294 (2025).
  33. Zuffanelli, S. et al. Analysis of the Split Ring Resonator (SRR) antenna applied to passive UHF-RFID tag design. *IEEE Trans. Antennas Propag.* **64**, 856–864 (2016).
  34. Islam, M. R. et al. Tri circle split-ring resonator-shaped metamaterial with mathematical modeling for oil concentration sensing. *IEEE Access* **9**, 161087–161102 (2021).
  35. Jahan, I. et al. Two split rings resonator-based perfect metamaterial absorbers with the incident and polarization angle independent for sensing applications. *J. Magn. Magn. Mater.* **594**, 171904 (2024).
  36. Baena, J. D. et al. Equivalent-circuit models for split-ring resonators and complementary split-ring resonators coupled to planar transmission lines. *IEEE Trans. Microw. Theory Tech.* **53**, 1451–1460 (2005).
  37. Khan, M. I., Fraz, Q. & Tahir, F. A. Ultra-wideband cross polarization conversion metasurface insensitive to incidence angle. *J. Appl. Phys.* **121**, 045103 (2017).
  38. Kim, S. et al. An RFID-enabled inkjet-printed soil moisture sensor on paper for “smart” agricultural applications. In *Proc. IEEE SENSORS 1507–1510* (IEEE, 2014).
  39. da Fonseca, N. S. S. M., Freire, R. C. S., Batista, A., Fontgalland, G. & Tedjini, S. A passive capacitive soil moisture and environment temperature UHF RFID based sensor for low cost agricultural applications. In *Proc. SBMO/IEEE MTT-S International Microwave and Optoelectronics Conference (IMOC) 1–4* (IEEE, 2017).
  40. Budalal, A. A. H., Islam, M. R., Abdullah, K. & Abdul Rahman, T. Modification of distance factor in rain attenuation prediction for short-range millimeter-wave links. *IEEE Antennas Wirel. Propag. Lett.* **19**, 1027–1031 (2020).
  41. Ma, Z. & Chen, J. Adaptive path planning method for UAVs in complex environments. *Int. J. Appl. Earth Obs. Geoinf.* **115**, 103133 (2022).
  42. Olshevsky, V. & Sakhnovich, L. Matched filtering for generalized stationary processes. *IEEE Trans. Inf. Theory* **51**, 3308–3313 (2005).
  43. Alahnomi, R. A., Zakaria, Z., Ruslan, E., Ab Rashid, S. R. & Mohd Bahar, A. A. High-Q sensor based on symmetrical split ring resonator with spurlines for solids material detection. *IEEE Sens J.* **17**, 2766–2775 (2017).
  44. Li, L., Bai, Y., Li, L., Wang, S. & Zhang, T. A superhydrophobic smart coating for flexible and wearable sensing electronics. *Adv. Mater.* **29**, 1702517 (2017).
  45. Diao, J. & Warnick, K. F. Poynting streamlines, effective area shape, and the design of superdirective antennas. *IEEE Trans. Antennas Propag.* **65**, 861–866 (2017).
  46. Chen, S., Zhong, S., Yang, S. & Wang, X. A multiantenna RFID reader with blind adaptive beamforming. *IEEE Internet Things J.* **3**, 986–996 (2016).
  47. Huang, Z. et al. Frequency division multiple access extension of standard UHF RFID systems for multiple tags inventory with successive interference cancellation. *IEEE Internet Things J.* **12**, 19615–19630 (2025).
  48. Mamabolo, E. et al. Application of precision agriculture technologies for crop protection and soil health. *Smart Agric. Technol.* **12**, 100808 (2025).
  49. Ramesh, Y. et al. A smart nail platform for wireless subsoil health monitoring via unmanned aerial vehicle-assisted radio frequency interrogation. HARVEST Subsoil Health Monitoring, <https://doi.org/10.5281/zenodo.17819189> (2025).
- Manufacturing Aware and Responsive Thin Films (R.R.), National Institute of Diabetes and Digestive and Kidney Diseases program at the National Institutes of Health (IR21DK128715-01A1) (R.R.), and National Institute of Food and Agriculture (13699514) (R.R.). The authors would also like to acknowledge the support staff and engineers of Birck Nanotechnology Center, School of Electrical and Computer Engineering, and School of Materials Engineering at Purdue University.

### Author contributions

Y.R., M.M.R., S.G., P.S., A.K., S.A., and R.R. conceived the idea and designed the research. Y.R., M.M.R., and S.G. contributed to the antenna design, data communication architecture, methodology development, validation, data curation, and initial manuscript drafting. P.S. and M.M.R. were responsible for the hardware implementation of the wireless reader system, software development, and system-level validation. A.K. and Y.R. performed soil protocol development and conducted both in-lab and field characterizations. J.A. provided resources and facilitated in-field measurements. Y.R., M.M.R., S.G., A.K., and R.R. contributed to writing, reviewing, and editing the manuscript, including figures and plots preparation. R.R. led the project, supervised the work, secured funding, administered the project, and performed final review and editing.

### Competing interests

The authors declare no competing interests.

### Additional information

**Supplementary information** The online version contains supplementary material available at <https://doi.org/10.1038/s41467-025-67889-w>.

**Correspondence** and requests for materials should be addressed to Rahim Rahimi.

**Peer review information** *Nature Communications* thanks Rosdiadee Nordin and the other, anonymous, reviewer(s) for their contribution to the peer review of this work. A peer review file is available.

**Reprints and permissions information** is available at <http://www.nature.com/reprints>

**Publisher's note** Springer Nature remains neutral with regard to jurisdictional claims in published maps and institutional affiliations.

**Open Access** This article is licensed under a Creative Commons Attribution-NonCommercial-NoDerivatives 4.0 International License, which permits any non-commercial use, sharing, distribution and reproduction in any medium or format, as long as you give appropriate credit to the original author(s) and the source, provide a link to the Creative Commons licence, and indicate if you modified the licensed material. You do not have permission under this licence to share adapted material derived from this article or parts of it. The images or other third party material in this article are included in the article's Creative Commons licence, unless indicated otherwise in a credit line to the material. If material is not included in the article's Creative Commons licence and your intended use is not permitted by statutory regulation or exceeds the permitted use, you will need to obtain permission directly from the copyright holder. To view a copy of this licence, visit <http://creativecommons.org/licenses/by-nc-nd/4.0/>.

© The Author(s) 2025

### Acknowledgements

The authors would like to acknowledge the funding support from Wabash Heartland Innovation Network (WHIN), Scalable

<sup>1</sup>School of Electrical and Computer Engineering, Purdue University, West Lafayette, IN, USA. <sup>2</sup>Birck Nanotechnology Center, Purdue University, West Lafayette, IN, USA. <sup>3</sup>Indiana Corn and Soybean Innovation Center, Purdue University, West Lafayette, IN, USA. <sup>4</sup>Department of Agronomy, Purdue University, West Lafayette, IN, USA. <sup>5</sup>School of Materials Engineering, Purdue University, West Lafayette, IN, USA. <sup>6</sup>These authors contributed equally: Yashwanth Ramesh, Muhammad Masud Rana. ✉ e-mail: [rrahimi@purdue.edu](mailto:rrahimi@purdue.edu)